PCCP

PAPER

View Article Online
View Journal | View Issue



Cite this: *Phys. Chem. Chem. Phys.*, 2025, **27**, 15213

# Effect of thermal treatments on high surface area anatase $TiO_2$†

Chiara Nannuzzi, ‡*[a] Ton V. W. Janssens[b] and Gloria Berlier *[a]

Received 8th May 2025,
Accepted 28th June 2025

DOI: 10.1039/d5cp01731a

rsc.li/pccp

Titanium dioxide ($TiO_2$) is widely employed in catalysis, energy conversion, and environmental applications, where high surface area and crystallinity play crucial roles in enhancing performance. However, achieving thermal stability while maintaining these properties remains challenging. This study investigates the structural and textural evolution of a high-surface-area anatase $TiO_2$ subjected to various thermal treatments, including vacuum, static, and flow conditions. Through $N_2$ adsorption, X-ray diffraction, electron microscopy, and *in situ* infrared spectroscopy, we elucidate the interplay between surface area, crystal growth, surface sites and exposed crystallographic surfaces. Thermal treatments in vacuum preserve the surface area up to 450 °C, while static calcination leads to significant reduction and scarce reproducibility. Controlled flow conditions improve stability, though humidity accelerates sintering. Spectroscopic analyses reveal a strong interaction with water, influencing hydroxylation and dehydroxylation dynamics. Our findings provide insights into optimizing $TiO_2$ processing conditions for applications requiring high thermal stability and catalytic efficiency.



## Introduction

Titanium dioxide ($TiO_2$) is a versatile material with a wide array of applications ranging from photocatalysis, solar energy harvesting, and environmental remediation to its roles in sensors, catalysis, and biomedicine. Its exceptional electrical, optical, and photocatalytic properties arise from its strong oxidation and reduction potential when exposed to photon energy.[1,2] These characteristics make $TiO_2$ a critical material for addressing global challenges in sustainable energy and environmental protection.

$TiO_2$ is one of the most studied materials, and many synthetic approaches have been developed in the years to obtain materials with different crystal phase, particle dimension and morphology.[1,3–5]

A particularly important property of $TiO_2$'s functionality is its surface area, which significantly influences its efficiency in applications such as heterogeneous catalysis, photocatalysis, and dye-sensitized solar cells (DSSCs).[4,6–8] High-surface-area $TiO_2$ enhances interaction with reactants, facilitates charge transfer processes, and increases the density of active sites, which are essential for improved catalytic and photoactive performance.[9,10] Despite these advantages, challenges remain in synthesizing $TiO_2$ presenting at the same time high crystallinity and large surface area, as traditional methods often require trade-offs between these attributes. Approaches such as hydrothermal treatments and templated synthesis have shown promise in addressing these challenges by enabling controlled manipulation of morphology and crystalline phases.[11–13]

High surface area $TiO_2$ materials are typically characterized by low thermal stability, resulting in a loss of surface area as a result of particle agglomeration and consequential sintering, often accompanied by the transition of anatase to the most stable rutile phase.[1,3,14–16] One example of application is the use of $TiO_2$ as support for $VO_x$ based catalysts for the $NH_3$-based Selective Catalytic Reduction ($NH_3$-SCR), which is used for the removal of $NO_x$ in the exhaust gas treatment of light-duty and heavy-duty diesel vehicles.[17–20] Notwithstanding their low cost and better tolerance to $SO_2$ poisoning, $VO_x/TiO_2$ catalysts display lower activity with respect to Cu-exchanged zeolites in the low temperature range (between 150 and 300 °C).[19,21–23] One approach to improve the catalyst activity is to increase the surface area of the support, which turns in increases the number of active sites.[24] A thermal treatment is necessary during the synthesis of $VO_x/TiO_2$ catalysts, to decompose the precursor of the $VO_x$ active phase (ammonium metavanadate or other vanadium salts). It is clear that a high surface area $TiO_2$ support can be used to improve $VO_x/TiO_2$ activity provided that it is stable during the synthesis and in reaction conditions. This means that the use of a high surface area $TiO_2$

[a] *Department of Chemistry, NIS and INSTM Centers, Università di Torino, via P. Giuria 7, 10125 Turin, Italy. E-mail: chiara.nannuzzi2@unibo.it, gloria.berlier@unito.it*
[b] *Umicore ApS, kogle Allè 1, 2970 Hørsholm, Denmark*

† Electronic supplementary information (ESI) available. See DOI: https://doi.org/10.1039/d5cp01731a

‡ Current address: CIRI-FRAME, University of Bologna, viale Ciro Menotti 48, 48122 Marina di Ravenna, Italy.

requires a preliminary investigation of the changes induced by thermal treatments on morphology, crystal phase, surface area, and porosity for all the applications which requires preliminary thermal treatments and/or high temperature operational conditions.

This work focuses on the characterization of high-surface-area anatase $TiO_2$, exploring the interplay between surface area, crystallinity, and surface sites distribution as a function of different thermal treatments. The aim is to provide insights into the relationship between atomic surface structure and structural/textural parameters, and to optimize the experimental conditions to obtain a stable high-surface-area $TiO_2$ with enhanced performance and applicability across a broad spectrum of scientific and industrial domains.

## Experimental

### Materials and methods

The $TiO_2$ materials studied in this work were supplied by Umicore ApS Denmark.[24]

The specific surface areas (SSA) of $TiO_2$ as such and thermally treated in different conditions was determined from the $N_2$ adsorption isotherms at liquid nitrogen temperature with ASAP 2020 Micromeritics instrument, and according to the Brunauer–Emmett–Teller (BET) equation. The pore dimensions were determined with the Barrett–Joyner–Halenda (BJH) equation on the adsorption curve. In some case, pore size distribution was calculated by the DFT tool available in the Microactive software (Micromeritics), using the classical type, cylinder geometry, and the $N_2$ Harkins and Jura thickness curve. Before the $N_2$ adsorption measurements, the samples were outgassed at room temperature (RT), until a residual pressure of $1 \times 10^{-1}$ mbar was reached and heated in vacuum for 2 h at different temperatures.

A Nabertherm LT muffle was used for calcination in static conditions, in a temperature range between 100 and 500 °C, for 1 or 5 h. A tubular Carbolite furnace was used for flow conditions treatments at 350 °C in dry and wet air (synthetic air bottle was used, with the addition of water in the case of wet condition). In this case a total flow of 150 mL $min^{-1}$ was used. TGA measurements were performed with thermogravimetric analyzer TA-Q600, with 100 mL $min^{-1}$ flow of air. About 20 mg of each sample was analyzed in $Al_2O_3$ pans. Equilibration at 30 °C for 30 minutes was set before heating up to 900 °C, with a ramp of 5 °C $min^{-1}$. Weights were normalized to 100% after removal of physisorbed water at 150 °C.

X-ray diffraction patterns were collected with a PANalytical X'Pert Pro powder diffractometer, equipped with a X'Celerator detector, using Cu Kα (1.5418 Å) radiation generated at 45 kV and 40 mA. The patterns were measured in the $2\theta$ range from 20–85°, with a step size of 0.017° and a counting time of 120 seconds per step; Bragg–Brentano geometry was used with $\frac{1}{4}$ slits. Before the measurements, all samples were soft-milled and positioned in the sample holder carefully to avoid preferential orientations. The crystal domains ($d$) along [101], [001], and [100] directions were calculated with Scherrer equation, where $K$ is a shape factor (in this study 0.9), $\lambda$ is the X-ray wavelength, $B_{exp}$ is the experimental peak width at half maximum (FWHM) at the given $2\theta$, $B_{ins}$ is the instrumental broadening (measured on Si reference in the same analysis condition), and $\theta$ is the measured Bragg angle in radians. In the calculation of the FWHM, used in the Scherrer equation: $d = \frac{K\lambda}{(B_{exp} - B_{ins})\cos\theta}$, the broadening in the 35–40 $2\theta$ range corresponding to the (004) reflection is associated with a significant error in the estimation of the crystallite dimension along the $c$-axis, due to the overlapping with the (103) and (112) reflections. To obtain a more accurate value for the width of the (004) reflection, this range was fitted with three pseudo-Voigt profiles located at 37.03° (103), 37.89° (004), and 38.66° (112); the angle positions were taken from the anatase $TiO_2$ PDF reference (ICDD PDF 00-021-1272).

Information on the morphology of the $TiO_2$ particles was obtained by electron microscopy. High-resolution transmission electron microscopy (HR-TEM) was performed on a JEOL 3010-UHR microscope operated at 300 kV, using samples of $TiO_2$ dispersed on Cu grids covered in lacey carbon. Samples were suspended in water and sonicated for 30 minutes before performing the measurements.

Fourier transform infrared (IR) experiments were carried out on samples pressed into thin self-supporting pellets for transmission measurements. The pellets were fixed in a gold frame, and placed inside an *in situ* IR cell, which allows carrying out thermal treatments in vacuum, performing low-temperature measurements and controlling the gas atmosphere. The spectra were measured in transmission mode with 4 $cm^{-1}$ resolution on a Bruker N Invenio spectrophotometer equipped with a mercury cadmium telluride (MCT) cryodetector. Backgrounds and sample spectra were recorded measuring 128 interferogram scans to achieve a good signal-to-noise ratio. All the reported spectra were normalized by using the optical density of prepared pellets (weight of pellet divided by area), to correct for possible variations in the thickness of the pellets.

The nature and distribution of surface sites were investigated using CO as probe molecule. Before introducing CO, the samples were treated at 500 °C for 3 h under dynamic vacuum to maintain a residual pressure of $5 \times 10^{-4}$ mbar, before exposure to 80 mbar of $O_2$. After 10 min in $O_2$ the samples were cooled to 150 °C, where $O_2$ was removed, and then further cooled to room temperature. Then the sample was moved to the spectrophotometer, cooled down with liquid nitrogen and 40 mbar of CO were introduced into the cell. To study the CO stretching region ($\nu$CO), the spectra recorded after CO adsorption were processed by subtracting the spectra collected prior to the exposure. The relative amount of different surface sites was evaluated by fitting the corresponding components with Lorentz/Gaussian curves with the OPUS software. The calculated areas were normalized to the optical densities. The results are compared with those obtained on an anatase $TiO_2$ with similar morphology and lower surface area (ls-$TiO_2$, 89 $m^2$ $g^{-1}$).[24]

*In situ* IR experiments during thermal treatments in gas flow were performed with the Aabspec cell. A total flow of 50 mL

 

$min^{-1}$ (synthetic air $N_2$ + 20% $O_2$) was used for these experiments and the temperature ramp was set at 5 °C $min^{-1}$.

## Results and discussion

### Raw material (r-$TiO_2$)

The textural properties of r-$TiO_2$ material, that is surface area (SSA) and pore size and volume, were obtained from the $N_2$ adsorption measurements. Before performing the measure, r-$TiO_2$ was outgassed at room temperature, to avoid possible changes induced by thermal treatments. The isotherm and pore distribution curves of r-$TiO_2$ are reported in Fig. 1. The isotherm can be classified as type IV with a broad hysteresis loop starting around $p/p^0$ = 0.6, with SSA of 345 $m^2\ g^{-1}$ and pore volume of 0.35 $cm^3\ g^{-1}$ (Table 1). A narrow pore size distribution centered around 20 Å is observed, a value close to the limit for the validity of the BJH method, and confirmed by DFT analysis. In other words, the raw material has pores at the borderline between micro and mesopores.

The X-ray diffraction pattern of r-$TiO_2$, reported in black in Fig. 2, only shows the anatase phase, with a non-complete crystallinity, indicated by the broadening of the peaks, together with the non-flat baseline. In particular, the three reflections in the 35–40 2$\theta$ range are convoluted in a single broad peak. The average size of crystal domains ($d$) along the [101], [001] and [100] directions were determined using the Scherrer equation, from the (101), (004) and (200) anatase reflections, resulting in values of 6, 3, and 8 nm along $b$, $c$ and $a$ directions, respectively. These dimensions can be ascribed to an elongated shape along the $b$ and $a$ axes, suggesting a platelet-like morphology.[1,25–27]

Transmission electron microscopy (TEM) was used to investigate the morphology of r-$TiO_2$ material (Fig. 3). The sample was dispersed in $H_2O$ and sonicated, but this treatment was not sufficient to avoid a high degree of agglomeration. Due to agglomeration, it is very difficult to distinguish single particles in order to obtain information on the exposed crystal planes. On the whole, a qualitative analysis- not detailed in the manuscript- was performed using Gatan DigitalMicrograph software to obtain the interplanar distances of the families of planes giving diffraction, which were then compared to those of anatase $TiO_2$ (ICDD PDF file 00-021-1272). This analysis revealed a high relative amount of the (101) plane, followed by (001) and (100), respectively. Nevertheless, it was possible to estimate the particles' dimensions, around 5 nm, from high magnification images (right panel of Fig. 3), in good agreement with the crystallite dimensions obtained with the Scherrer analysis.

Table 1 Textural properties of r-$TiO_2$ after different thermal treatments in vacuum in the measurement cell

| Sample | Temperature (°C) | SSA ($m^2\ g^{-1}$) | Pore size (Å) | Pore volume ($cm^3\ g^{-1}$) |
|---|---|---|---|---|
| r-$TiO_2$ | RT | 345 | ~20 | 0.35 |
| 150v-$TiO_2$ | 150 | 390 | ~20 | 0.36 |
| 200v-$TiO_2$ | 200 | 385 | ~20 | 0.37 |
| 350v-$TiO_2$ | 350 | 355 | ~20 | 0.32 |
| 450v-$TiO_2$ | 450 | 312 | ~20 | 0.37 |

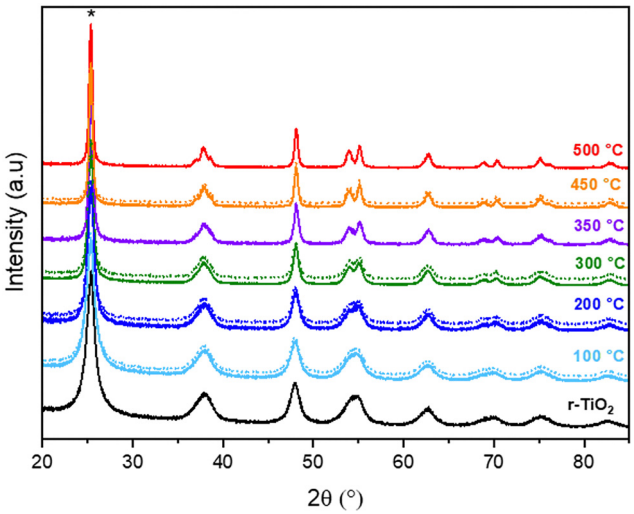


Fig. 2 XRD patterns in 20–85 2$\theta$ range of r-$TiO_2$ as such and after calcination in static conditions at different temperatures, for 5 and 1 h (full and dotted curves, respectively). Patterns are normalized for the (101) diffraction peak of anatase $TiO_2$ labeled with * and vertically translated for clarity.

### Effect of thermal treatments

High surface area $TiO_2$ materials are typically characterized by low thermal stability, resulting in a loss of surface area as a

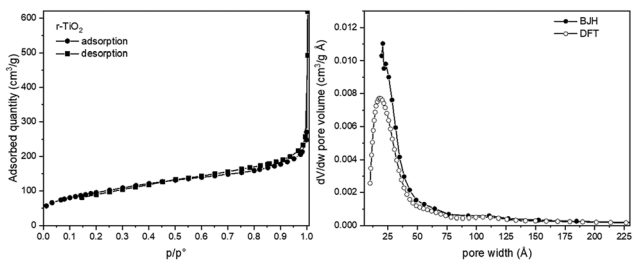


Fig. 1 $N_2$ sorption isotherm of r-$TiO_2$ outgassed at room temperature and corresponding pore size distribution, calculated by BJH and DFT (left and right, respectively).

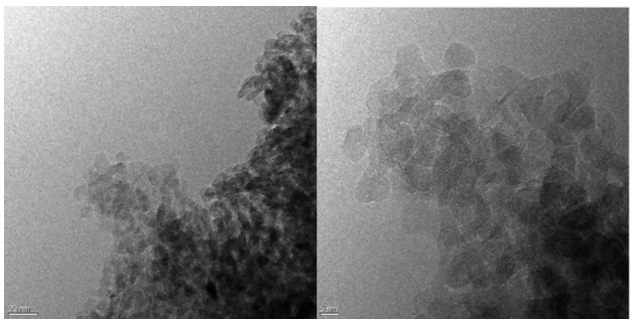

Fig. 3 HR-TEM images at low and high magnification, left and right respectively, of r-$TiO_2$.

result of particle agglomeration and consequential sintering, often accompanied by the transition of anatase to the most stable rutile phase.[1,3,14,15] Since many applications require temperatures higher than room temperature, we have studied the effect of thermal treatments in different conditions on crystallinity, textural properties and surface sites distribution.

Thermal treatments were carried out in vacuum (directly in the cell used for $N_2$ adsorption measurements, without exposure to atmosphere), in static muffle and in flow conditions. The resulting samples are labeled as *xy*-$TiO_2$, where *x* is the temperature used in the treatment and *y* is the condition (v as vacuum, s as static). Dry- and wet-$TiO_2$ refer to samples thermally treated in flow conditions at 350 °C (see below).

### Vacuum conditions

The r-$TiO_2$ material was studied after pre-treatments performed in vacuum before the $N_2$ adsorption measurements, directly in the measurement cell. The textural properties resulting from treatments at different temperatures are listed in Table 1. The corresponding isotherms are reported in Fig. S1 in the ESI.†

The results show an increase of SSA after mild thermal treatments (150 and 200 °C), with respect to r-$TiO_2$ outgassed at room temperature. This could be explained by the desorption of physisorbed water that was not removed by room temperature outgassing. The SSA starts to decrease with respect to 150v- and 200v-$TiO_2$ after thermal treatments at 350 and 450 °C. However, thermal treatments in vacuum did not affect the porosity, both in terms of pores distribution and pore volume.

### Static conditions

The results described in the previous section show that thermal treatments in vacuum only slightly affect the textural properties of the high surface area material up to 450 °C. However, this kind of treatment is not suitable for large scale applications, also considering the fact that thermal treatments are one of the main bottlenecks for companies in terms of costs and energy consumption. Thus, calcination in a static oven was performed at different temperatures, for 1 or 5 h.

For each temperature, the length of the treatment does not particularly affect the shape of the XRD patterns, in terms of peak intensity and widths. Crystallinity is increasing with increasing temperature, already with the treatment at 200 °C, thus, the gradual increase in the size of the crystalline domains in all the samples (Table 2). The two peaks in the 51–57 2$\theta$ interval starts to be resolved at 300 °C, while the three peaks between 35–40 2$\theta$, become resolved only after the treatment at 450 °C. The observed preferential growth of the crystallites along *a* and *b* directions, observed for r-$TiO_2$, is maintained after the thermal treatments. The anatase structure is preserved up to 500 °C, without the formation of extra-phases in appreciable amounts. Particle size after thermal treatments at 450/500 °C is comparable to the anatase particles in the benchmark P25 $TiO_2$ sample (26 nm).[27]

While the length of the thermal treatment only slightly affects the diffraction pattern and particle size, this parameter seems to have more effect on the textural properties. The $N_2$ sorption isotherms and pore size distribution of a selection of samples are reported in Fig. 4. The isotherms measured on samples treated in the 300–450 °C temperature range show differences particularly at high $p/p^0$ values, that is in the range corresponding to capillary condensation in mesopores. In fact, the considered samples show distinct pore size distributions, as evidenced in the right panel of Fig. 4. The measured surface areas and porosity parameters are resumed in Table 3. Both temperature and length of the treatment affect SSA and pore size, but some discrepancies are observed. The surface area increases from 300 to 350 °C after 1 h treatment, from 152 to 172 $cm^2\ g^{-1}$, while it does not significantly change when the treatment was carried out for 5 h. The treatment at 350 °C for 5 h was repeated, leading to a different surface area. Generally, the thermal treatments in this temperature range cause a clear change in the pore size, which becomes larger and less homogeneous, particularly in the case of the sample treated at 450 °C for 5 h. This change does not sensibly affect the pore volume with respect to pristine r-$TiO_2$, which was characterized by a narrow distribution of pores around 20 Å. This could be related to agglomeration and sintering of $TiO_2$ particles during thermal treatments, where a large number of small pores condense in a lower number of larger ones. To explore this aspect, pore size distribution was calculated by DFT (Fig. S2, ESI†). The samples treated at 350 and 450 °C for 5 h show a bimodal distribution, with a fraction of pores around 25 Å and a broader distribution of bigger pores.

In general, these results suggest a low control and reproducibility of textural properties when the thermal treatment is

Table 2 Crystallite dimensions along *b*, *c*, and *a* direction obtained with Scherrer equation for r-$TiO_2$ samples treated in static conditions at different temperatures and time lengths

| Sample | Length (h) | $d_{101}$ (nm) | $d_{004}$ (nm) | $d_{200}$ (nm) |
|---|---|---|---|---|
| 100s-$TiO_2$ | 1 | 7 | 4 | 9 |
| | 5 | 7 | 5 | 9 |
| 200s-$TiO_2$ | 1 | 10 | 7 | 10 |
| | 5 | 10 | 7 | 10 |
| 300s-$TiO_2$ | 1 | 13 | 6 | 14 |
| | 5 | 14 | 7 | 15 |
| 350s-$TiO_2$ | 5 | 17 | 8 | 18 |
| 450s-$TiO_2$ | 1 | 17 | 9 | 18 |
| | 5 | 21 | 15 | 24 |
| 500s-$TiO_2$ | 5 | 23 | 15 | 24 |

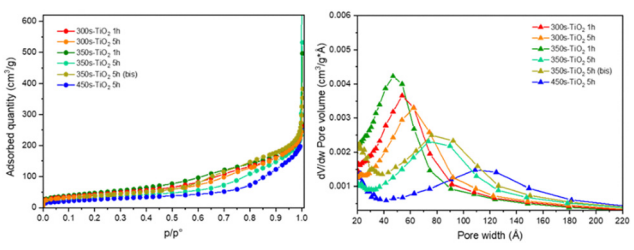


Fig. 4 $N_2$ sorption isotherms and corresponding BJH pore size distribution (left and right panels, respectively), after calcination in static conditions at different temperature and time lengths. For sake of clarity only the adsorption curves have been plotted.

 

Table 3 Textural properties of r-$TiO_2$ after different thermal treatments in static conditions. The treatment at 350 °C for 5 h has been repeated twice

| Sample | Length (h) | SSA ($m^2$ $g^{-1}$) | Pore size (Å) | Pore volume ($cm^3$ $g^{-1}$) |
|---|---|---|---|---|
| 300s-$TiO_2$ | 1 | 152 | 55 | 0.35 |
| | 5 | 140 | 62 | 0.36 |
| 350s-$TiO_2$ | 1 | 172 | 50 | 0.36 |
| | 5 | 138 | 23, 80 | 0.37 |
| | 5 | 116 | 27, 80 | 0.34 |
| 450s-$TiO_2$ | 5 | 97 | 23, 120 | 0.31 |

carried out in static conditions, as will be further discussed in the following.

### Flow conditions

The discrepancies and low reproducibility observed after treatments in static conditions could be related to variations in the ambient conditions, specifically regarding air humidity. To verify this hypothesis, thermal treatments were carried out in controlled atmosphere in flow conditions. Specifically, dry and wet (3% $H_2O$) air flows were used for the treatment of r-$TiO_2$ at 350 °C for 1 h. The choice of the parameters was made with the aim to minimize the loss in surface area caused by the thermal treatment, which appears to be more consistent at higher temperature. Moreover, this temperature was found to be sufficient for the decomposition of the ammonium metavanadate salt used as a precursor of $VO_x$ in the synthesis of $VO_x$/$TiO_2$ catalysts and relevant for the application of these catalysts in the $NH_3$-SCR reaction.[24]

Surface area, porosity, and crystalline domain size measured after the treatments are reported in Table 4. The corresponding experimental data are shown in Fig. S3 and S4 (ESI†). To check for reproducibility, the treatment was performed three times for each condition. Values of surface area and porosity were found to be consistent, with variations well within the experimental error (5% for BET surface area), indicating a good reproducibility for this method, at variance with what was obtained in static conditions.

The surface area changes with the flow composition: in particular, the presence of $H_2O$ leads to a higher decrease in the surface area than the dry flow. However, the pore volume does not significantly change in the different conditions. The decrease of surface area with the wet flow is associated to an increase of the pore size, which moves from around 48 to 62 nm, with a small broadening of the size distribution (Fig. S3, right panel, ESI†). Calcination in dry air flow was also carried out at 300 °C for 1 h (not reported), resulting in a similar surface area (183 $m^2$ $g^{-1}$).

As discussed above, the FWHM of (101), (004), and (200) diffraction peaks (XRD patterns reported in Fig. S4, ESI†) were used in the Scherrer equation to obtain the crystal domains along *b*, *c*, and *a* axes, respectively (Table 4), and similar dimensions were obtained in the two cases.

In summary, the data show that the presence of $H_2O$ vapor during the thermal treatment negatively affects surface area, the decrease of which has been related to the sintering of the nanoparticles,[1] also confirmed by the increase in the crystallite dimensions along *a* and *b* axes (see Table 4).

This supports the hypothesis that the low reproducibility of the results obtained after thermal treatments in static conditions without environmental control are related to variations of humidity, and could explain why the treatments in vacuum have a lower impact on the material textural properties.

Table 4 Surface area, pore volume and crystalline domains calculated with Scherrer equation for r-$TiO_2$ calcined at 350 °C for 1 h in dry and wet air flows. SSA is averaged of three experiments

| Sample | SSA ($m^2$ $g^{-1}$) | Pore size (Å) | Pore volume ($cm^3$ $g^{-1}$) | $d_{101}$ (nm) | $d_{004}$ (nm) | $d_{200}$ (nm) |
|---|---|---|---|---|---|---|
| Dry-$TiO_2$ | 182 ± 1 | 48 ± 1 | 0.36 ± 0.01 | 12 | 7 | 12 |
| Wet-$TiO_2$ | 148 ± 3 | 62 ± 2 | 0.36 ± 0.01 | 13 | 7 | 13 |

### Surface sites

The results discussed so far indicates that the thermal treatments applied to the r-$TiO_2$ sample yield different outcomes in terms of textural properties and crystallite domains. Typically, a high surface area correlates with high defectivity represented by OH groups and undercoordinated $Ti^{4+}$ sites located on steps, edges, and corners of the particles.[28–30] Therefore, it is crucial to examine the surface sites of the r-$TiO_2$ material. The use of CO molecules as probe followed by IR spectroscopy is one of the most commonly employed technique for this purpose.[27,28,30–33]

To obtain reliable results, ensuring a bare and clean surface of the material before sending the CO probe is essential, as this allows for direct interaction between the CO molecules and the surface sites. This implies that a thermal treatment is required to remove the physisorbed water, followed by oxidation at high temperatures to eliminate any organic matter present on the titanium oxide surface.[26,27,29,30,34]

In this study, we investigated the OH surface groups of r-$TiO_2$ during thermal treatments using *in situ* IR in flow conditions, and probed the different $Ti^{4+}$ sites with CO molecules after a thermal treatment in vacuum.

The r-$TiO_2$ was heated in air flow, from room temperature to 500 °C, with a 1 h hold at the final temperature. During the heating process, IR spectra were recorded every minute in order to track changes in the OH population. The collected spectra, displayed in Fig. 5, show the $\nu$OH region (3800–2400 $cm^{-1}$) and the bending ($\delta$) H–O–H mode of physisorbed water (1800–1500 $cm^{-1}$)[35] in the left and right panel, respectively.

At 100 °C (dark green spectrum), the IR spectra exhibit a broad and intense band (out of scale) centered at 3200 $cm^{-1}$, characteristic of hydrogen-bonding interactions among water molecules and between water molecules and surface OH groups.[36] As the temperature increases, the absorption gradually decreases, revealing the typical features of surface Ti–OH groups. By 150 °C, three distinct peaks at 3630, 3655, and 3679 $cm^{-1}$ emerged. These features merged into two less-resolved components (light green spectra form 300 °C) showing a maximum at 3662 $cm^{-1}$ and a shoulder at 3681 $cm^{-1}$. By

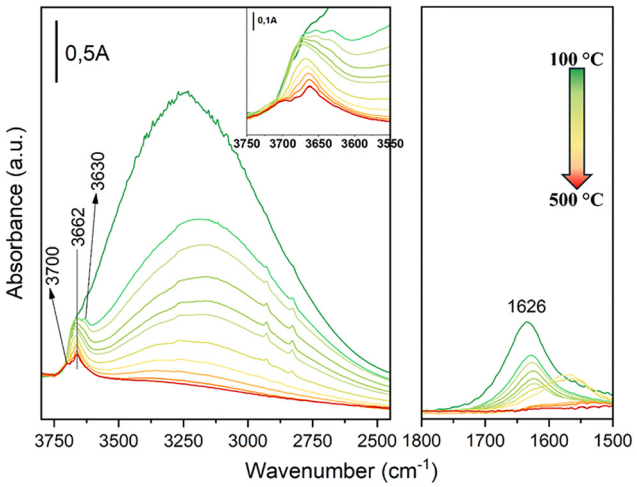


Fig. 5 *In situ* IR spectra of r-$TiO_2$ during thermal treatment in air flow, from 25 °C to 500 °C. Total flow 50 mL $min^{-1}$, ramp 5 °C $min^{-1}$.

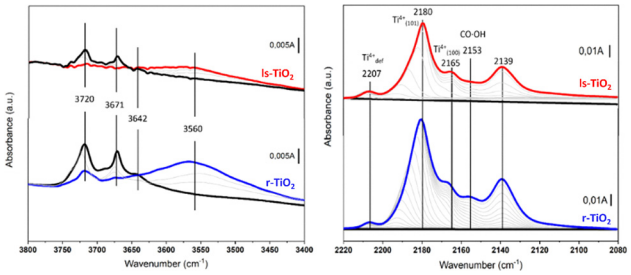


Fig. 6 Normalized IR spectra of CO adsorption (40 mbar) on r-$TiO_2$ in the $\nu$OH and $\nu$CO regions, left and right panels, respectively (bottom, blue). For comparison the top curves (red) show the corresponding spectra measured on a low surface area $TiO_2$ (ls-$TiO_2$) with similar properties (see text). The left panel also reports the spectra of both $TiO_2$ before CO adsorption, after thermal treatment in vacuum in vacuum at 500 °C for 3 h followed by oxidation. These spectra were used as a reference to obtain the background subtracted spectra reported in the right panel. Spectra normalized with respect to the pellet thickness.

further increasing the temperature, the shoulder decreased in intensity, and a new component appeared at higher frequencies (3700 $cm^{-1}$) at 450 °C. Beyond this temperature, only a decrease in the whole intensity was observed.

The three peaks observed at 150 °C can be attributed to weakly/strongly H-bonded OH groups which dehydroxylate at increasing temperatures, releasing water molecules. This leads to the appearance of free OH groups that vibrate at higher frequencies, 3700 and 3681 $cm^{-1}$, located on edges, vertices and corners, and extended surfaces of the $TiO_2$ particles.[37,38] Notice that the positions of these bands is slightly different with respect to what measured at low temperature (see below). In the right panel, the intensity of the $\delta$ H–O–H mode peak at 1626 $cm^{-1}$ indicates the presence of $H_2O$ on the surface of r-$TiO_2$. As the temperature increased, the intensity of this peak decreased due to water desorption, with the complete disappearance of the signal at 450 °C, coinciding with the emergence of isolated OH groups.

Next, we studied the $Ti^{4+}$ surface sites by CO adsorption monitored by IR spectroscopy, after a pretreatment in vacuum at 500 °C for 3 h, followed by oxidation in 80 mbar of $O_2$ for 10 minutes (Fig. 6). This procedure was optimized after several trials (not reported), to remove strongly adsorbed water molecules. Following this treatment, the surface area of r-$TiO_2$ decreased to 227 $m^2\ g^{-1}$, representing a 34/42% reduction from the initial SSA value measured after RT/150 °C vacuum treatment, respectively (see Table 1). For comparison, we report the spectra obtained in the same conditions on an anatase $TiO_2$ with similar morphology and surface area of 89 $m^2\ g^{-1}$ (labelled as low surface area $TiO_2$, ls-$TiO_2$). The main properties of this material are summarized in Table S1 and Fig. S5 (ESI†).

The spectroscopic fingerprints of the two $TiO_2$ in the $\nu$OH region are reported in the left panel of Fig. 6. Two main features are located at 3720 and 3671 $cm^{-1}$, corresponding to isolated Ti–OH in the vertices and edges, and bridged Ti–OH–Ti sites on extended surfaces, respectively.[37,39–41] On r-$TiO_2$ two clear shoulders are observed at higher and lower frequency with respect to the main peaks, at 3740 and 3642 $cm^{-1}$. The former is attributed to OH groups on the (001) surface, formed by a dissociative adsorption of $H_2O$.[42–44] The latter, also detected in the *in situ* experiment (see Fig. 5), indicates that some $H_2O$ molecules are adsorbed on the (101) surface, in accordance with Arrouvel *et al.*, suggesting a density $\leq$10.8 $H_2O/nm^2$.[42] This is also in agreement with the weak signal at 1620 $cm^{-1}$ related to the bending mode of $H_2O$[36] persisted in r-$TiO_2$ after the pretreatment (not reported), indicating the difficulty in the removal all the physisorbed $H_2O$ in this sample.

When CO is admitted, the OH groups weakly interact with it, forming OH···CO adducts, observed as a broad band centered at 3560 $cm^{-1}$. However, while bridged Ti–OH–Ti are almost completely involved in the interaction, isolated Ti–OH ones are less affected, in line with a lower acidity.[39]

Moving to the $\nu$CO region (right panel of Fig. 6), the main peak at 2180 $cm^{-1}$ is assigned to CO interacting with 5-fold-coordinated $Ti^{4+}$ ions located on the extended (101) facet, while at 2165 $cm^{-1}$ the interaction between CO and $Ti^{4+}$ on the (100) facets is observed.[28,31,33,45,46] The peak at 2153 $cm^{-1}$ corresponds to CO interacting with OH groups, while the peak at 2139 $cm^{-1}$ is attributed to liquid-like form of adsorbed CO, which does not imply specific interactions with $TiO_2$.[32,33,47] The signal related to CO interaction with defective $Ti^{4+}$ sites is located at relatively high frequency (2207 $cm^{-1}$) and is associated with 4-fold or 3-fold $Ti^{4+}$ sites located on steps, edges, and corners on high-index crystal planes.[27,48] No information can be obtained on the presence and extension of the (001) surface since the interaction of CO with the corresponding $Ti^{4+}$ sites can be observed only at lower temperature.[25,31]

More interesting is the comparison of the relative concentration of surface sites in the two samples with similar morphology and different surface areas. Focusing on the $\nu$CO bands, the area of the different components related to $Ti^{4+}$···CO on different surfaces or defects, described above, has been calculated after curve fitting (Table S2, ESI†). Based on this, we calculated the ratio of the different surface sites in the two samples (Table 5).

 

Table 5 Relative ratio of different surfaces sites on r-$TiO_2$ and ls-$TiO_2$ estimated from IR spectra in the $\nu$OH and $\nu$CO regions

| Surface sites | Ratio r-$TiO_2$/ls-$TiO_2$ |
|---|---|
| Defects | 2.4 |
| (101) | 1.4 |
| (100) | 4.7 |
| Total $Ti^{4+}$ | 1.6 |
| OH | 3.4 |

Looking into the single components, the ratio between the estimated amount of defective sites in the two samples reflects the ratio between surface areas (2.4 *vs.* 2.6), agreeing with the association between this textural property and the defectivity of the material. This does not hold for the probed $Ti^{4+}$ sites on the (101) facets (2180 $cm^{-1}$). This can be in part explained by the persistence of some adsorbed water molecules in the high surface area material (see above, band at 3642 $cm^{-1}$) and also indicates that this surface, which is the most stable surface on anatase,[1] is less extended in the irregular particles of r-$TiO_2$. Indeed, we observe a higher relative concentration of $Ti^{4+}$ on (100) (band at 2165 $cm^{-1}$), which supports the hypothesis that the small particles of the high surface area materials exposes different preferential surfaces, even if both samples show the same preferential elongation along the *c*-axis (Table 2 and Table S1, ESI†). This hypothesis is further supported by the ratio between the total probed $Ti^{4+}$ sites (1.6). Since in the tested conditions it is not possible to monitor the $Ti^{4+}$ sites on the (001) surface, it is reasonable to assume that this surface has a large extension on ls-$TiO_2$, in agreement with the observation of the $\nu$OH component at 3740 $cm^{-1}$ attributed to OH groups from a dissociative adsorption of $H_2O$ on the (001) surface.[42–44] Finally, the ratio between the integrated areas of OH groups in the two samples greatly exceeds the ratio between surface areas (Table 5). However, this value could be overestimated, due to the presence in r-$TiO_2$ of the two components at 3740 and 3642 $cm^{-1}$ related to $H_2O$ adsorption.

In this work, we investigated the changes in the textural properties and surface sites of an high surface area anatase $TiO_2$ after thermal treatments in different conditions. Our findings demonstrate that the surface area of r-$TiO_2$ is highly dependent on the specific treatment protocol and conditions, that is using a static oven, a tubular flow furnace (under dry or wet air), or vacuum treatments (*e.g.* in the BET cell or in the IR procedure).

Thermal treatments under vacuum had a minimal impact on the surface area and porosity of r-$TiO_2$ up to 450 °C, with the highest surface area (390 $m^2\ g^{-1}$) measured after outgassing at 150 °C, suggesting that heating in vacuum tends to preserve the material's surface area. However, a significant decrease in the surface area (227 $m^2\ g^{-1}$) was observed after the vacuum treatment at 500 °C, necessary for IR studies. This is important for understanding parameters that influence aggregation and sintering, as well as for semiquantitative considerations in IR spectra analysis. Notice that this was not observed for the reference ls-$TiO_2$ material, which preserved its surface area after the same treatment (89 $m^2\ g^{-1}$).

In contrast, treatments in oven under static conditions posed challenges in terms of reproducibility and sensitivity to treatment duration. Calcination at 300 °C resulted in a notable decrease in surface area, with values of 152 and 140 $m^2\ g^{-1}$ for 1 and 5 h, respectively, representing a 61 and 64% loss compared to the initial value of 390 $m^2\ g^{-1}$. Moreover, 1 h of calcination at 350 °C led to a higher surface area of 172 $m^2\ g^{-1}$ overcoming the measure error of 5%. After 450 °C and for longer calcination, a further decrease up to 97 $m^2\ g^{-1}$ was detected. The decrease in surface area is associated with an increase in crystal size domains, as calculated by the Scherrer equation. Some of the data measured after thermal treatments around 350 °C indicate scarce control and reproducibility under static conditions. These inconsistencies may stem on variations in humidity. To address this, calcination in a tubular oven in dry flow was carried out at the fixed temperature of 350 °C. By applying these conditions, higher reproducibility was obtained. Additionally, the presence of $H_2O$ was found to promote $TiO_2$ sintering, as evidenced by a slight increase in crystal domain size and a decrease in surface area to 145 $m^2\ g^{-1}$, corresponding to a 20% reduction compared to dry conditions (181 $m^2\ g^{-1}$).

Scherrer analysis provided crucial insights into the morphology of the r-$TiO_2$ samples, which cannot be analyzed in depth by TEM, due to the high agglomeration of the particles. By analyzing the growth along different crystallographic axes, the elongated shapes were attributed to a platelet-like morphology, in analogy with what observed for ls-$TiO_2$.[24]

The *in situ* IR study of r-$TiO_2$ during heating in air flow revealed a strong interaction between water and surface sites, which, considering the morphology, stands with the presence of extended (001) surfaces that strongly interact with water.[25,31,49] This surface is also responsible for dissociating $H_2O$ into the corresponding OH groups, which are stable up to 450 °C (shoulder at 3642 $cm^{-1}$).

Furthermore, CO adsorption at low temperature was followed by IR to analyze the material surface sites. The surface sites probed by CO adsorption, as shown in Fig. 6, were similar in both materials, with the main difference related to their intensity (Table 5). A high surface area generally correlates with an increased number of defective sites and OH groups. The former is confirmed by the semiquantitative analysis performed by the integration of the corresponding IR peaks (2207 $cm^{-1}$) in r-$TiO_2$ and in a benchmark anatase $TiO_2$ sample (ls-$TiO_2$) with a SSA of 89 $m^2\ g^{-1}$ (see Table 5). As for the latter, the measured amount is markedly higher with respect to what expected on the basis of surface area, but also includes contributions from dissociated and strongly adsorbed $H_2O$ molecules. Moreover, the lower relative amount of $Ti^{4+}$ sites on the main anatase (101) surface (2180 $cm^{-1}$) coupled to the higher relative amount of $Ti^{4+}$ sites on (100) (2165 $cm^{-1}$) and the indirect indication about a significant extension of the (001) surface, testified by Scherrer analysis performed on XRD pattern and the presence of OH groups vibrating at higher frequencies, points to a higher contribution of typically less abundant facets in r-$TiO_2$ material with respect to what

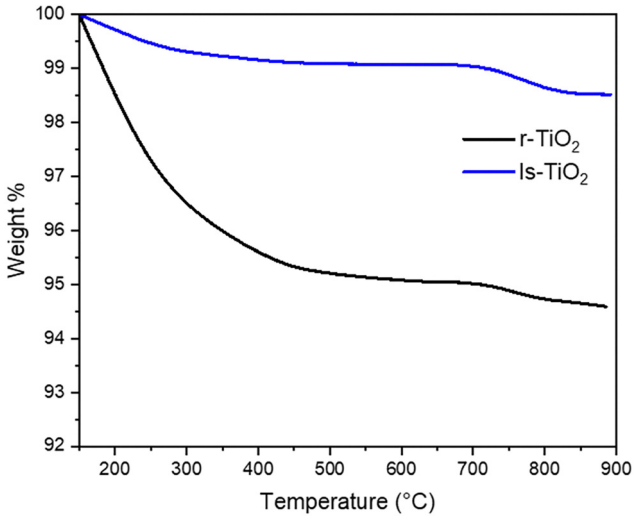


Fig. 7 TGA curves of ls-$TiO_2$ (blue) and r-$TiO_2$ (black) heated in air flow. Weights were normalized to 100% to the dry weight of the material, after the loss of physisorbed water between 30 and 150 °C. Heating rate 5 °C $min^{-1}$.

expected on anatase[1,31,40] and observed on a 'standard' ls-$TiO_2$ sample. This feature can be related to the smaller particle size of r-$TiO_2$ ($\approx$5 nm).

$TiO_2$ were analyzed by thermogravimetric analysis in the 150–900 °C range (Fig. 7). r-$TiO_2$ shows a large weight loss between 30 and 150 °C, accounting for *ca.* 15% of dry weight, *vs. ca.* 1.3% in ls-$TiO_2$ (Fig. S6, ESI†). This could suggest a higher hydrophilicity of r-$TiO_2$, since the amount of physisorbed water is not proportional to surface area.

The data reported in Fig. 7 were thus normalized with respect to the dry weight measured after heating at 150 °C.

After water desorption, ls-$TiO_2$ shows $a \approx 1.8\%$ weight loss up to 900 °C, which can be related to dehydroxylation, that is water through a condensation reaction between surface Ti–OH groups.

The extent of dehydroxylation is higher in r-$TiO_2$, resulting in a total weight loss of *ca.* 7.6%. This result closely aligns with the surface area ratio of 4.4 (390 *vs.* 89 $m^2$ $g^{-1}$), indicating that the amount of OH groups on the surface is directly proportional to the surface area.

For both materials, most of the dehydroxylation takes place up to 500 °C, which is the temperature used in the pretreatment for the *in situ* IR study. Again, this is more evident for r-$TiO_2$, and suggests that the decrease in surface area observed by high temperature treatments is related to dehydroxylation involving vicinal particles, ruling the aggregation and sintering process.

## Conclusions

The findings of this study highlight the significant influence of thermal treatments on the textural properties of an high surface area anatase $TiO_2$, labeled as r-$TiO_2$. Increasing the treatment temperature consistently led to a gradual reduction in surface area, while extending the treatment duration from 1 to 5 h under static conditions caused an even greater decrease. Vacuum pre-treatment before BET measurements resulted in a smaller surface area reduction compared to other methods, particularly those involving a static oven, which produced lower surface area values and scarce reproducibility of the results. In contrast, thermal treatments under flow conditions, more suitable for industrial applications, offered better reproducibility and generally higher surface areas with respect to treatments in static oven. The presence of $H_2O$ in the flow was found to promote sintering, leading to a slight increase in crystal domain size and a more pronounced surface area reduction, further corroborating results obtained from static calcination.

Although the high degree of agglomeration hindered an in depth analysis of r-$TiO_2$ morphology, combining Scherrer analysis with TEM suggested an elongated, platelet-like morphology, in analogy with a benchmark anatase $TiO_2$ sample with lower surface area (ls-$TiO_2$). *In situ* IR spectroscopy during thermal heating provided valuable insights into the behavior of OH groups as temperature increased, with three distinct H-bonded OH groups converting into free OH groups located on edges, vertices, corners and extended surfaces after water desorption at 450 °C. The high temperature indicates a strong water interaction with surface sites, particularly on the (101) and (001) facets.

CO adsorption followed by IR allowed us to provide a qualitative description of $TiO_2$ surface sites in the high surface area material, and to compare the concentration of defects (4-fold and 3-fold $Ti^{4+}$ sites at steps, edges, and corners) and the extension of preferential surfaces with respect to the benchmark material. The results point to a higher contribution of typically less abundant facets, that is (100) and (001), in the r-$TiO_2$ material. Particularly, the presence of a significant amount of the (001) is indicated by the strong resistance of the OH groups formed by dissociative adsorption of $H_2O$ observed in the material (band at 3740 $cm^{-1}$).

Finally, TGA analysis confirmed that the amount of OH groups on r-$TiO_2$ is proportional to surface area, by comparison to the benchmark ls-$TiO_2$ sample. Under heating in flow in TGA, ls-$TiO_2$ undergoes a severe dehydroxylation, reaching a concentration of OH groups similar to the low surface area material around 500 °C, as confirmed by IR spectroscopy. The severe dehydroxylation can be related to the thermal instability of the material, probably occurring during the aggregation and sintering processes leading to a decrease in surface area.

## Conflicts of interest

There are no conflicts to declare.

## Data availability

The data supporting this article have been included as part of the ESI.†

 

## Acknowledgements

C. Nannuzzi and G. Berlier acknowledge support from the Project CH4.0 under the MUR program ''Dipartimenti di Eccellenza 2023–2027'' (CUP: D13C22003520001).

## References

1 U. Diebold, *Surf. Sci. Rep.*, 2003, **48**, 53–229.
2 T. Peng, D. Zhao, K. Dai, W. Shi and K. Hirao, *J. Phys. Chem. B*, 2005, **109**, 4947–4952.
3 S. Reghunath, D. Pinheiro and S. D. KR, *Appl. Surf. Sci. Adv.*, 2021, **3**, 100063.
4 R. Zhang, A. A. Elzatahry, S. S. Al-Deyab and D. Zhao, *Nano Today*, 2012, **7**, 344–366.
5 M. Bankmann, R. Brand, B. H. Engler and J. Ohmer, *Catal. Today*, 1992, **14**, 225–242.
6 H. J. Snaith and L. Schmidt-Mende, *Adv. Mater.*, 2007, **19**, 3187–3200.
7 V. Dhas, S. Muduli, S. Agarkar, A. Rana, B. Hannoyer, R. Banerjee and S. Ogale, *Sol. Energy*, 2011, **85**, 1213–1219.
8 Y. V. Kolen'ko, B. R. Churagulov, M. Kunst, L. Mazerolles and C. Colbeau-Justin, *Appl. Catal., B*, 2004, **54**, 51–58.
9 J. Bisquert, D. Cahen, G. Hodes, S. Ruhle and A. Zaban, *J. Phys. Chem. B*, 2004, **108**, 8106–8118.
10 T. Fröschl, U. Hörmann, P. Kubiak, G. Kucerová, M. Pfanzelt, C. K. Weiss, R. J. Behm, N. Hüsing, U. Kaiser, K. Landfester and M. Wohlfahrt-Mehrens, *Chem. Soc. Rev.*, 2012, **41**, 5313–5360.
11 D. S. Kim and S. Y. Kwak, *Appl. Catal., A*, 2007, **323**, 110–118.
12 G. Colón, M. C. Hidalgo and J. A. Navío, *Catal. Today*, 2002, **76**, 91–101.
13 Y. Dai, S. Shen, Z. Ma, L. Ma, Z. Sun, J. Yu, C. Wan, S. Han, D. Mao and G. Lu, *J. Nanosci. Nanotechnol.*, 2017, **17**, 3772–3778.
14 J. Krýsa, M. Keppert, J. Jirkovský, V. Štengl and J. Šubrt, *Mater. Chem. Phys.*, 2004, **86**, 333–339.
15 T. V. Nguyen, H. C. Lee and O. B. Yang, *Sol. Energy Mater. Sol. Cells*, 2006, **90**, 967–981.
16 V. N. Koparde and P. T. Cummings, *ACS Nano*, 2008, **2**, 1620–1624.
17 E. Tronconi and I. Nova, *Urea-SCR Technology for deNOx After Treatment of Diesel Exhausts*, Springer International Publishing, 2014.
18 K. Skalska, J. S. Miller and S. Ledakowicz, *Sci. Total Environ.*, 2010, **408**, 3976–3989.
19 L. Han, S. Cai, M. Gao, J. Hasegawa, P. Wang, J. Zhang, L. Shi and D. Zhang, *Chem. Rev.*, 2019, **119**, 10916–10976.
20 Z. Shi, Q. Peng, E. J. iaqiang, B. Xie, J. Wei, R. Yin and G. Fu, *Fuel*, 2023, **331**, 125885.
21 A. J. Shih, I. Khurana, H. Li, J. González, A. Kumar, C. Paolucci, T. M. Lardinois, C. B. Jones, J. D. Albarracin Caballero, K. Kamasamudram, A. Yezerets, W. N. Delgass, J. T. Miller, A. L. Villa, W. F. Schneider, R. Gounder and F. H. Ribeiro, *Appl. Catal., A*, 2019, **574**, 122–131.
22 J. P. Dunn, H. G. Stenger and I. E. Wachs, *Catal. Today*, 1999, **51**, 301–318.
23 M. Qing, S. Su, L. Wang, L. Liu, K. Xu, L. He, X. Jun, S. Hu, Y. Wang and J. Xiang, *Chem. Eng. J.*, 2019, **361**, 1215–1224.
24 C. Nannuzzi, L. Mino, S. Bordiga, A. H. Pedersen, J. M. Houghton, P. N. R. Vennestrøm, T. V. W. Janssens and G. Berlier, *J. Catal.*, 2023, **421**, 228–239.
25 K. Bourikas, C. Kordulis and A. Lycourghiotis, *Chem. Rev.*, 2014, **114**, 9754–9823.
26 L. Mino, F. Pellegrino, S. Rades, J. Radnik, V. Hodoroaba, G. Spoto, V. Maurino and G. Martra, *ACS Appl. Nano Mater.*, 2018, **1**, 5355–5365.
27 L. Mino, G. Spoto, S. Bordiga and A. Zecchina, *J. Phys. Chem. C*, 2012, **116**, 17008–17018.
28 K. I. Hadjiivanov and D. G. Klissurski, *Chem. Soc. Rev.*, 1996, **25**, 61–69.
29 L. Mino, A. M. Ferrari, V. Lacivita, G. Spoto, S. Bordiga and A. Zecchina, *J. Phys. Chem. C*, 2011, **115**, 7694–7700.
30 A. Zecchina, D. Scarano, S. Bordiga, G. Ricchiardi, G. Spoto and F. Geobaldo, *Catal. Today*, 1996, **27**, 403–435.
31 L. Mino, A. M. Ferrari, V. Lacivita, G. Spoto, S. Bordiga and A. Zecchina, *J. Phys. Chem. C*, 2011, **115**, 7694–7700.
32 K. Hadjiivanov, J. Lamotte and J. C. Lavalley, *Langmuir*, 1997, **13**, 3374–3381.
33 K. I. Hadjiivanov and G. N. Vayssilov, *Adv. Catal.*, 2002, **47**, 307–511.
34 C. Deiana, M. Minella, G. Tabacchi, V. Maurino, E. Fois and G. Martra, *Phys. Chem. Chem. Phys.*, 2013, **15**, 307–315.
35 M. Takeuchi, L. Bertinetti, G. Martra, S. Coluccia and M. Anpo, *Appl. Catal., A*, 2006, **307**, 13–20.
36 N. B. Colthup, L. H. Daly and S. E. Wiberly, *Introduction to Infrared and Raman Spectroscopy*, New York, 2nd edn, 1975.
37 A. Mahdavi-Shakib, J. M. Arce-Ramos, R. N. Austin, T. J. Schwartz, L. C. Grabow and B. G. Frederick, *J. Phys. Chem. C*, 2019, **123**, 24533–24548.
38 A. A. Tsyganenko and V. N. Filimonov, *J. Mol. Struct.*, 1973, **19**, 579–589.
39 L. Mino, Á. Morales-García, S. T. Bromley and F. Illas, *Nanoscale*, 2021, **13**, 6577–6585.
40 S. Dzwigaj, C. Arrouvel, M. Breysse, C. Geantet, S. Inoue, H. Toulhoat and P. Raybaud, *J. Catal.*, 2005, **236**, 245–250.
41 K. Hadjiivanov, *Identification and Characterization of Surface Hydroxyl Groups by Infrared Spectroscopy*, Elsevier Inc., 1st edn, 2014, vol. 57.
42 C. Arrouvel, M. Digne, M. Breysse, H. Toulhoat and P. Raybaud, *J. Catal.*, 2004, **222**, 152–166.
43 A. Travert, O. V. Manoilova, A. A. Tsyganenko, F. Maugé and J. C. Lavalley, *J. Phys. Chem. B*, 2002, **106**, 1350–1362.
44 C. Morterra, *J. Chem. Soc.*, 1988, **84**, 1617–1637.
45 S. Pantaleone, F. Pellegrino, V. Maurino, M. Corno, P. Ugliengo and L. Mino, *J. Mater. Chem. A*, 2024, **12**, 4325–4332.
46 C. Morterra, E. Garrone, V. Bolis and B. Fubini, *Spectrochim. Acta, Part A*, 1987, **43**, 1577–1581.
47 A. A. Tsyganenko, L. A. Denisenko, S. M. Zverev and V. N. Filimonov, *J. Catal.*, 1985, **94**, 10–15.
48 H. Knozinger and S. Huber, *Faraday Trans.*, 1998, **94**(15), 2047–2059.
49 B. Zhang, F. Wei, Q. Wu, L. Piao, M. Liu and Z. Jin, *J. Phys. Chem. C*, 2015, **119**, 6094–6100.